Electronic Supplementary Material (ESI) for Lab on a Chip.

3D Printed Conformal Microfluidics for Isolation and Profiling of Biomarkers from Whole Organs

Supporting Information

Manjot Singh[a^], Yuxin Tong[a^], Kelly Webster[g], Ellen Cesewski[a,d], Alexander P. Haring[a,b], Sahil Laheri[a,c], Bill Carswell[f], Timothy O'Brien[e,f], Charles H. Aardema[e], Ryan S. Senger[f,h], John L. Robertson[e,f] and Blake N. Johnson[a,b,c,d,h*]

[a] Department of Industrial and Systems Engineering, Virginia Tech, Blacksburg, VA 24061 USA

[b] Macromolecules Innovation Institute, Virginia Tech, Blacksburg, VA 24061 USA

[c] School of Neuroscience, Virginia Tech Blacksburg, VA 24061 USA

[d] Department of Materials Science and Engineering, Virginia Tech, Blacksburg, VA 24061 USA

[e] School of Biomedical Engineering and Sciences, Virginia Tech, Blacksburg, VA 24061 USA

[f] Department of Biological Systems Engineering, Virginia Tech, Blacksburg, VA 24061 USA

[g] Department of Mechanical Engineering, Virginia Tech, Blacksburg, VA 24061 USA

[h] Department of Chemical Engineering, Virginia Tech, Blacksburg, VA 24061 USA

[^] These authors contributed equally to this work.

*Correspondence should be addressed to Blake N. Johnson (Telephone: (540) 231-0755; Fax: (540) 231-3322; Email: bnj@vt.edu)

1. Synopsis: This supporting information describes: the machine perfusion system (Fig. S1); the experimental setup for microfluidic biopsy measurements (Fig. S2); the experimental apparatus consisting of a structured-light scanner and 3D printing system (Fig. S3); Raman spectra of microfluidic biopsy samples and negative controls (Fig. S4); the 3D printing process for conformal microfluidic devices (Fig. S5); negative controls for comparison of device-organ 3D topography (Fig. S6); photographs of the 3D printed conformal microfluidic devices and device interface with whole organs (Fig. S7); additional computational fluid dynamic results (Figs. S8 and S9); photographs of device-microneedle integration for microfluidic biopsy measurements (Fig. S10); ELISA data for KIM-1 and β-actin in microfluidic biopsy samples (Fig. S11); supporting details on computational fluid dynamic calculations and simulations; and a video of flow visualization in the conformal microfluidic device (Vid. S1).

2. Supporting Calculations for Computational Fluid Dynamics Simulations: Given mass transfer from the organ surface into the microfluidic stream can be modelled as an internal flow problem and it has previously been reported that kidney tissue contains biomarkers (*e.g.*, the concentration of HSP-70 in kidney tissue has been reported to be ~275 ng/mL[1]), the mass flux (j) was modelled using a form of Newton's Law of Cooling for internal flow[2]:

$$j = k(c_s - c_m) \tag{1}$$

where k is the convective mass transfer coefficient, c_s is the surface concentration, and c_m is the mean (or bulk) fluid concentration at a given cross section. The mean concentration was assumed to be far less than the surface concentration (*i.e.*, $c_m << c_s$), and thus, was assumed to be zero in the calculation of the mass flux (an assumption that is supported by the simulation results). For example, the maximum bulk concentration was c_m = 16 pg/mL (measured at the outlet).

For laminar flow in a circular tube, the hydrodynamic entry length ($x_{d,v}$) is given as[2]:

$$x_{d,v} = 0.05ReD_h \tag{2}$$

where $Re = \rho v D_h/\mu$ is the Reynolds number, ρ is the fluid density, v is the average velocity of the fluid, $D_h = 4A/P$ is the hydraulic diameter, μ is the dynamic viscosity of the fluid, A is the cross-sectional area of the channel, and P is the wetted perimeter of the channel. Given the channel length (L) = 16 mm, $x_{d,v} \sim 140$ µm, which indicates the velocity profile in the channel is fully developed almost immediately after entry into the microchannel. Alternatively, for laminar flow in a circular tube, the thermal entry length ($x_{d,c}$) is given as[2]:

$$x_{d,c} = 0.05 ReScD_h \tag{3}$$

where $Sc = \upsilon/D$ is the Schmidt number, D diffusivity of HSP-70 in the fluid and $\upsilon = \mu/\rho$ is the kinematic viscosity of the fluid. Given the channel length (L) = 16 mm, $x_{d,c}$ = 1.27 m, which indicates the concentration profile does not reach a fully developed state before exiting the microchannel due to heat-mass transfer analogy.

The relative values of L, $x_{d,v}$, $x_{d,c}$ indicate the convective mass transfer regime within the microchannel corresponds to a fully developed velocity profile with an undeveloped concentration profile. Thus, to effectively model this convective mass transport problem, we use a corrected empirical convective mass transfer correlation for internal laminar flow in circular tubes subjected to a constant surface concentration condition developed by Sieder and Tate to calculate the convective mass transfer coefficient[2]:

$$\bar{Sh} = c_f 1.86 \left(\frac{ReSc}{L/D_h}\right)^{1/3} \left(\frac{\mu}{\mu_s}\right)^{0.14} \tag{4}$$

where $\bar{Sh} = kL/D$ is the average Sherwood number, μ_s is the dynamic viscosity of the fluid at the surface and c_f is a correction factor. The correction factor (c_f) was added to account for the fact that the original correlation developed by Sieder and Tate is for the case of constant surface concentration condition while the situation here is that of constant surface flux[2]. The correction factor was calculated as the ratio of Sh for constant surface flux to Sh for constant surface concentration for the case of fully developed flow (*i.e.*, c_f = 4.36/3.66)[2].

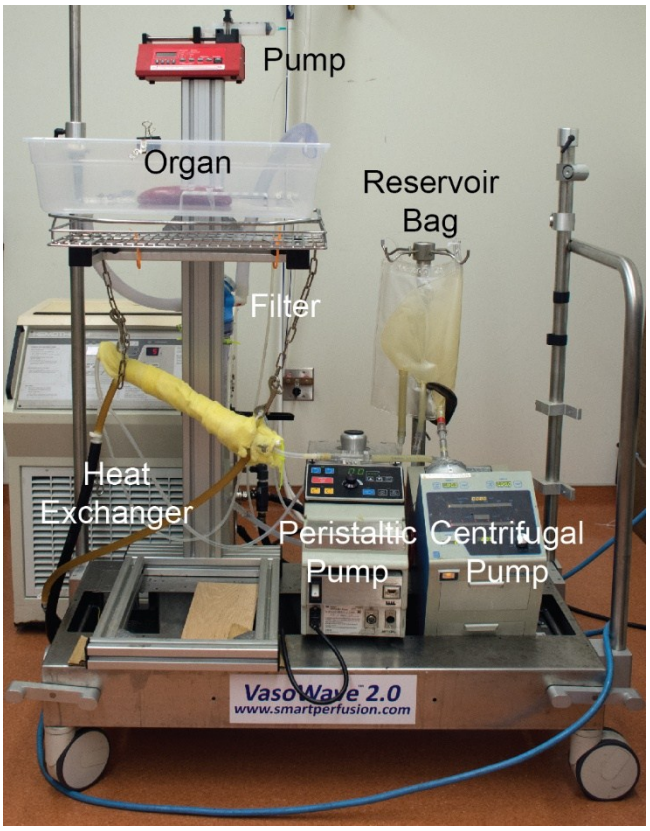

Figure S1: Hypothermic machine perfusion organ preservation system with its critical components highlighted.

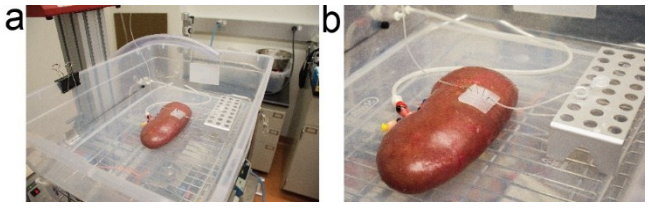

Figure S2: a) Photograph of a kidney undergoing microfluidic biopsy on the machine perfusion system described in **Fig. S1**. **b)** Close up view of panel **a**.

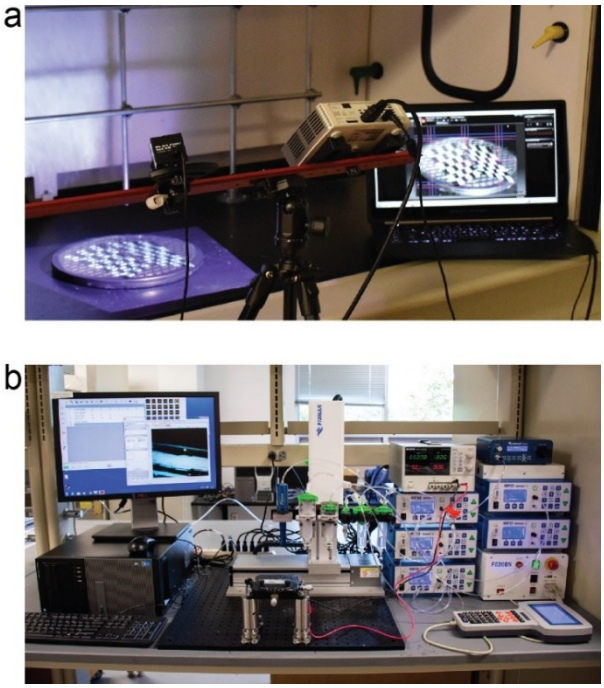

Figure S3: Structured-light scanning system for reverse engineering of kidney geometry (**a**) and microextrusion 3D printing system used for fabrication of 3D printed conformal microfluidic devices (**b**).

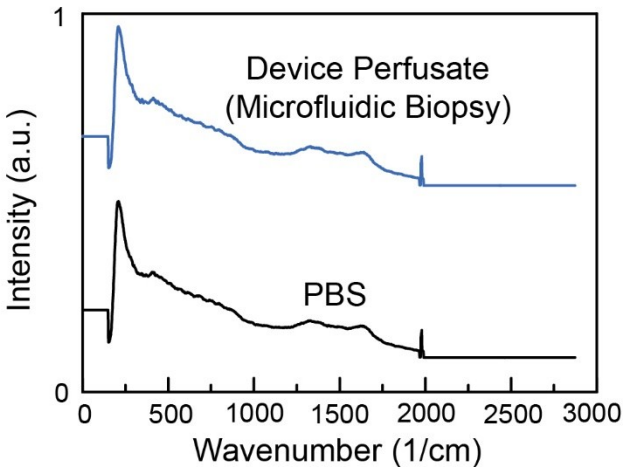

Figure S4: Representative Raman spectra of a microfluidic biopsy sample and negative control (PBS) used as the inputs for principal component analysis (PCA) and discriminant analysis of principal components (DAPC).

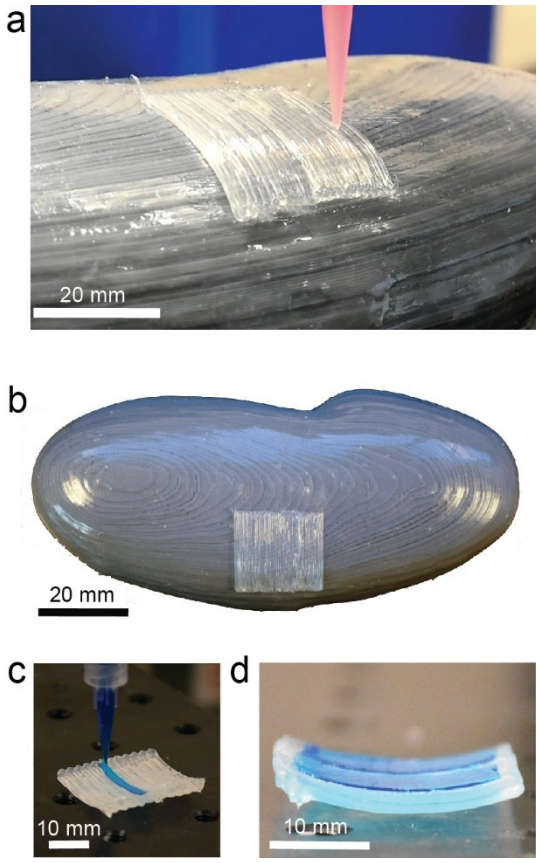

Figure S5: Photograph of the conformal microfluidic device printed on an anatomical substrate derived from medical imaging of porcine kidneys shown during the printing process (**a**) and post-printing (**b**). Photograph of the hydrogel adhesion layer of the conformal microfluidic device shown during the printing process (**c**) and post-printing (**d**) (blue dye used for visual contrast).

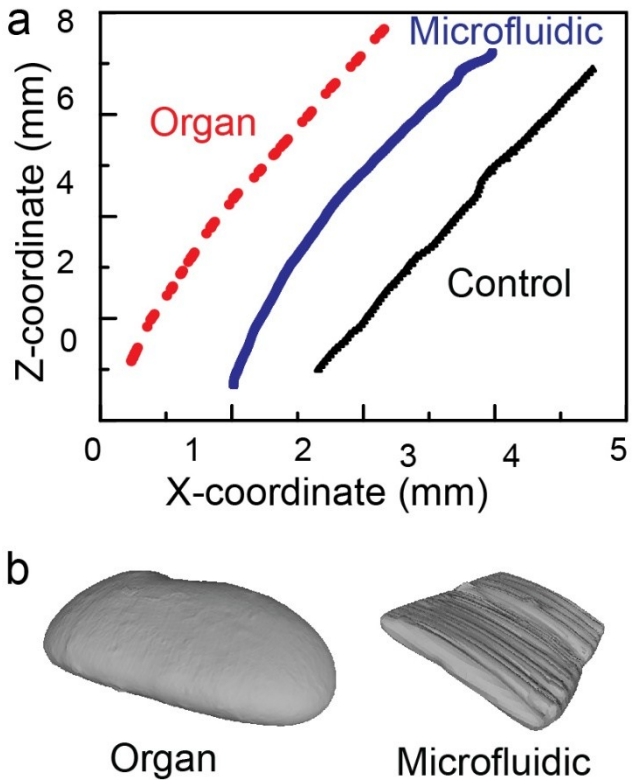

Figure S6: a) Curvilinear coordinate lines of the device and organ surface showing topographical matching between the 3D printed conformal microfluidic device and the organ surface at the scanned location. The control curve shows topographical data acquired from a non-conformal microfluidic device 3D printed on a flat non-biomimetic substrate to demonstrate the importance of the biomimetic conformal printing strategy on achieving topographical matching to the organ. **b)** Reverse engineered organ and device geometry obtained by structured-light scanning for comparison of topographical matching (data not to scale).

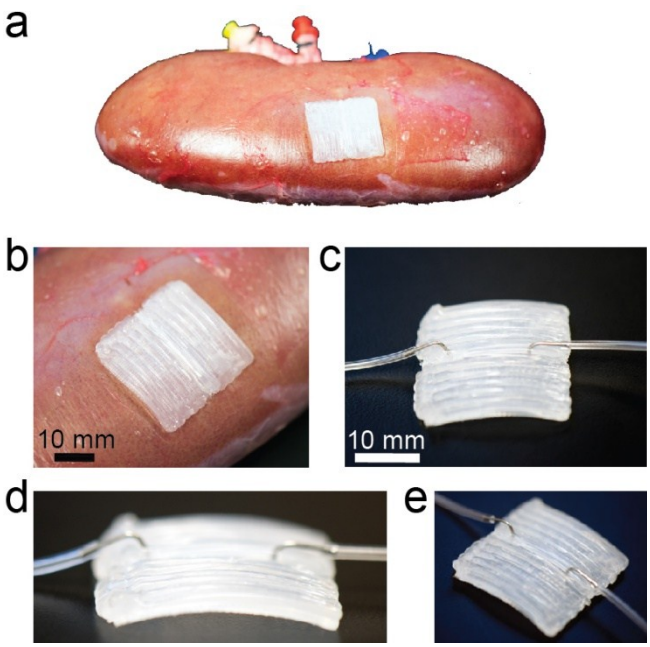

Figure S7: a) Photograph of a 3D printed conformal microfluidic device on a porcine kidney in the absence of supporting fluid handling components. **b)** Close up view of panel **a**. Additional photographs of 3D printed conformal microfluidic devices after integration of fluid handling components from top-down (**c**), side (**d**), and isometric (**e**) views.

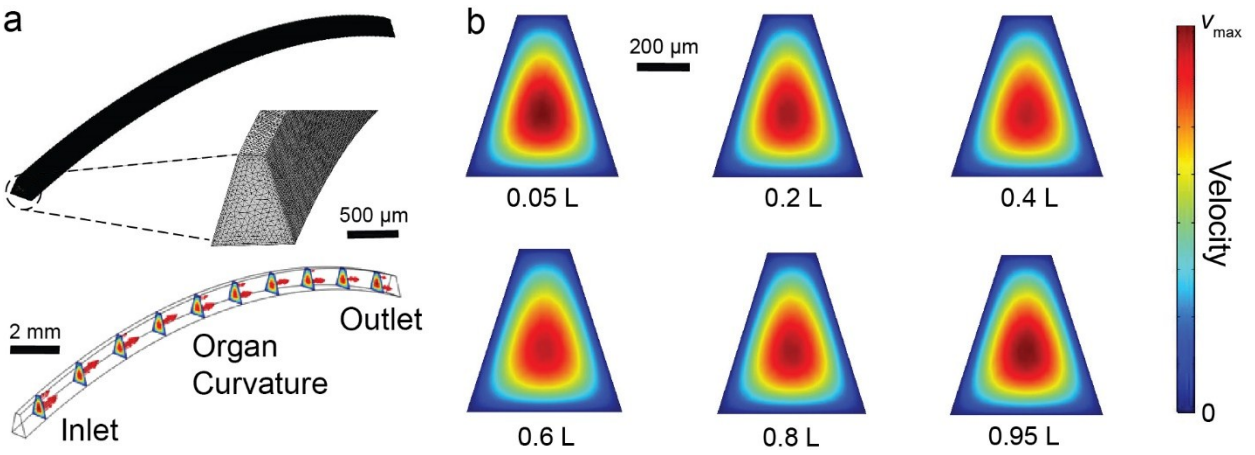

Figure S8: a) Meshed computational domain and slice-plot of the velocity profile shown throughout the conformal microchannel. **b)** Velocity profiles at different locations along the conformal microchannel (L = microchannel length).

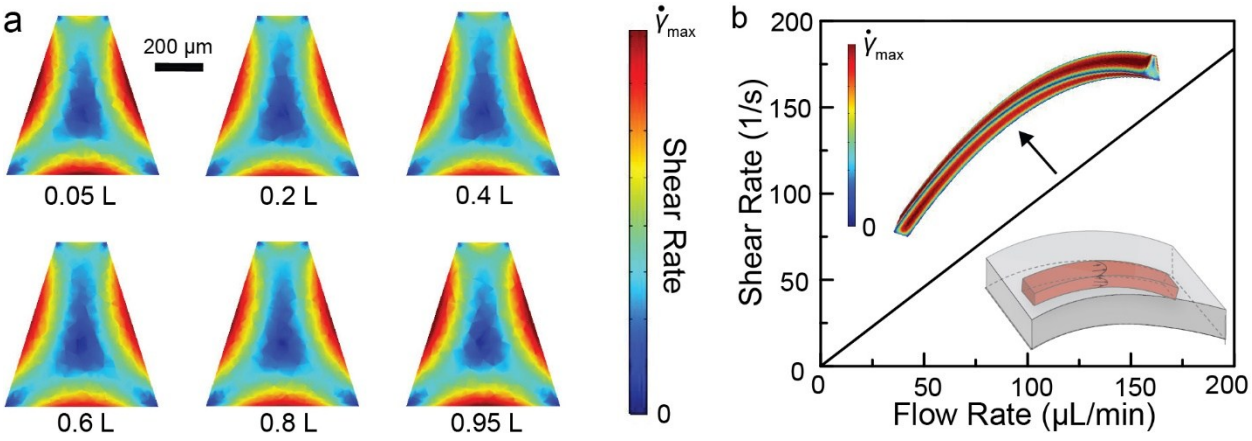

Figure S9: a) Shear rate profiles at different locations along the conformal microchannel (L = microchannel length). **b)** Integrated shear rate along the bottom of the conformal microfluidic channel (*i.e.*, the organ surface).

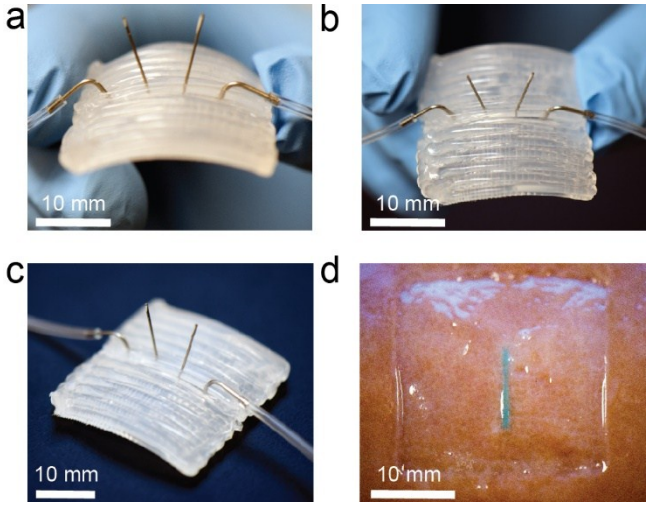

Figure S10: Photographs of microneedle integration with 3D printed microfluidic devices prior to interface with whole organs from side (**a**), top-down (**b**), and prismatic (**c**) views. **d)** Photograph of the organ surface after flushing the device with blue dye for approximately one minute showing tissue staining along the microfluidic channel contact area.

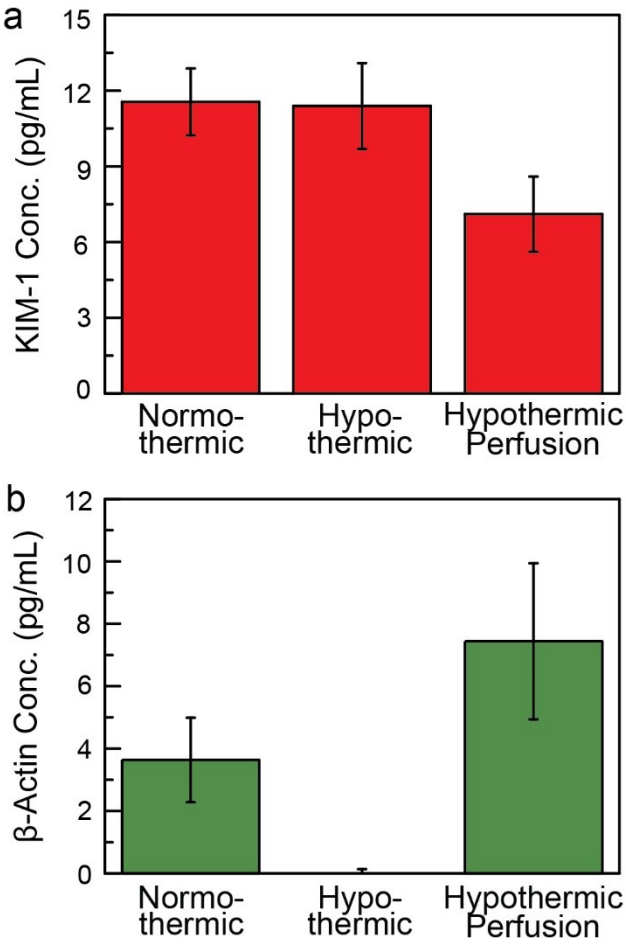

Figure S11: Measurements of KIM-1 (**a**) and β-actin (**b**) levels in microfluidic biopsy samples obtained by ELISA. The concentration of the KIM-1 was 12, 11, and 7 pg/mL for the normothermic group, the traditional cold storage hypothermic group, and the machine-perfused hypothermic group, respectively. The concentration of the β-actin was 4, 0, and 7 pg/mL for the normothermic group, the traditional cold storage hypothermic group, and the machine-perfused hypothermic group, respectively.

Video S1: Flow visualization in organ-conforming microfluidic devices using a blue dye (see file 'Video S1 - Flow visualization'). The video shows visualization of continuous flow through the 3D printed microfluidic device by switching between a PBS and a dye-containing PBS solution.

References

1. Rout, P.K., Kaushik, R. & Ramachandran, N. Differential expression pattern of heat shock protein 70 gene in tissues and heat stress phenotypes in goats during peak heat stress period. *Cell Stress Chaperon.* **21**, 645-651 (2016).
2. Incropera, F.P. & DeWitt, D.P. Fundamentals of Heat and Mass Transfer, Edn. Third Edition. (John Wiley & Sons).